JOURNAL OF GEOPHYSICAL RESEARCH, VOL. 98, NO. A9, PAGES 15,343–15,354, SEPTEMBER 1, 1993

Are Existing Magnetospheric Models Excessively Stretched?

MAURICIO PEREDO

Hughes STX Corporation at NASA/Goddard Space Flight Center, Laboratory for Extraterrestrial Physics, Greenbelt, Maryland

DAVID P. STERN AND NIKOLAI A. TSYGANENKO[1]

NASA/Goddard Space Flight Center, Laboratory for Extraterrestrial Physics, Greenbelt, Maryland

The distribution of the average north-south magnetic field component $\langle B_z \rangle$ in the vicinity of the neutral sheet has been investigated. This component is crucial for mappings between the nightside polar ionosphere and the equatorial magnetosphere. Data sets consisting of ~0.5 R_E averages of magnetic field observations by the IMP/HEOS and ISEE spacecraft have been compared to the field predicted by the Tsyganenko models T87 and T89. In agreement with recent studies by C. Huang (data with 4-s resolution), it was found that both T87 and T89 underestimate $\langle B_z \rangle$ in the near tail region (x_{GSM} = −10 to −22 R_E) by as much as a factor of 2. Modified versions of the T87 model, incorporating plasma sheet warping, were obtained by fitting the model parameters via nonlinear least squares to the ISEE data set and yielded $\langle B_z \rangle$ values in agreement with the ISEE data. The study reveals an enormous scatter among the observed baseline values of $\langle B_z \rangle$ (on a time scale of 10–20 min), as well as intrinsic biases imposed by the mathematical structure of tail models, and these two factors (especially the first one) greatly limit the accuracy of model predictions of tail $\langle B_z \rangle$. In order to reduce the second factor, a localized tail model has been developed and was used to explore the spatial variations of $\langle B_z \rangle$. Comparisons between observations and models, both global and local, are presented. Finally, suggested guidelines for use of existing models and limitations of their use are discussed.

1. INTRODUCTION

The Tsyganenko models [*Tsyganenko*, 1987*a*, 1989] (hereafter referred to as T87 and T89, respectively) are routinely used to trace connections between different magnetospheric regions and to correlate spacecraft measurements and ground-based observations. In what follows, designations such as T87 (or T87W, see below) and T89 will refer to the magnetic field expansion scheme, while designations such as T87*a* or T89*a* will mark particular implementations using different values for the model coefficients. Appendix A provides a summary of existing models, old and new, including key information regarding their derivation and expected domain of validity.

During the Fall 1990 AGU meeting, *Huang et al.* [1990] presented initial results from a study of ISEE observations suggesting that in the near-tail region, x_{GSM} = −10 to −22 R_E, Tsyganenko's T89 model underestimated the average north-south magnetic field component $\langle B_z \rangle$ by as much as a factor of 2. Accurate prediction of B_z in the plasma sheet is extremely important, since B_z strongly affects (1) the determination of the onset of nonadiabatic behavior of ions, (2) the mapping between ionospheric and magnetospheric features along magnetic field lines [*Rostoker and Skone*, 1992], and (3) the stress distribution in the tail.

Subsequent studies of the applicability of Tsyganenko's models to the magnetotail region yielded conflicting points of view. *Fairfield* [1991] compared Tsyganenko's 1982 model [*Tsyganenko and Usmanov*, 1982] and T87 to IMP/HEOS data and concluded that both models lacked sufficient tailward stretching of the magnetic field lines and that their values of $\langle B_z \rangle$ were too large. A similar conclusion regarding the T89 model was reported by *Kayser and Fairfield* [1991]. On the other hand, recent reports at AGU meetings [*Huang et al.*, 1991; *Peredo and Stern*, 1991*a*; *Tsyganenko et al.*, 1992; *Huang and Frank*, 1993] found that T87 and T89 underestimated $\langle B_z \rangle$ in the region x_{GSM} = −10 to −22 R_E and thus exhibited too much stretching in the near-tail region.

This paper examines the question in greater detail, concluding that in the region between x_{GSM} = −10 and −22 R_E, T89*b* yields only ~50–55% of the observed B_z while T87*b* gives ~80%. Following *Tsyganenko et al.* [1992], it is suggested here that the poor representation of $\langle B_z \rangle$ by the models arose, in part, because the IMP/HEOS data sets on which the original T87 and T89 models were based included relatively few data points from the equatorial tail region.

Global models based on least squares fitting of model parameters to a set of magnetic observations might possibly trade a poor fit in the plasma sheet region against improved fits in other regions of the magnetosphere. To avoid such problems, we have developed a local tail model to explore the spatial behavior of $\langle B_z \rangle$ in the plasma sheet region only.

2. TAIL $\langle B_z \rangle$ FROM DATA AND EXISTING MODELS

2.1. *Available Data Sets*

A modeling data base has been compiled by N. A. Tsyganenko [*Tsyganenko*, 1987*a*; *Tsyganenko et al.*, 1992]. The data sets have been labeled by the letters MDS, for Modeling Data Set, followed by the name of the observing spacecraft; for tail observations by the IMP spacecraft, a notation T or T2 has been appended to the name in order to differentiate data sets. These sets consisted of ~0.5 R_E

[1]Permanently at Institute of Physics, University of St. Petersburg, Russia.

Paper number 93JA01150.
0148-0227/93/93JA-01150$05.00

TABLE 1. Key Characteristics of Modeling Data Sets

Name and Origin of Data Set	Number of Points	Percent With AE Values	Percent With IMF Values	Percent With SW Plasma	Time Period
MDSIMP ($R < 17\ R_E$)					
Mead-Fairfield, 1975; Tsyganenko-Usmanov, 1982	12,616	100	53.0	51.4	July 1966 to March 1972
MDSHEOS					
Hedgecock and Thomas, 1975 Tsyganenko-Usmanov, 1982	6,265	100	58.7	63.1	Jan. 1969 to Aug. 1974
MDSIMPT					
NSSDC, Tsyganenko-Usmanov, 1980	10,891	90.9	63.9	54.3	Feb. 1964 to Nov. 1973
MDSIMPT2					
IMP-H and IMP-J; NSSDC, Tsyganenko-Usmanov, 1980	6,183	52.3	31.5	62.8	Sept. 1972 to March 1973 and Nov. 1973 to May 1980
MDSISEE					
Herbert and Elphic, 1986; NSSDC with Tsyganenko-Malkov, 1990	31,375	0 (for now)	85.1	92.5	Oct. 1977 to Dec. 1981

averages of magnetic field observations tagged with ancillary information on solar wind parameters (IMF and plasma data) and geomagnetic activity indices (*Kp*, *AE*, *Dst*). Key characteristics of the data sets are listed in Table 1. Several data sets have been used in this study. Our initial effort focused on exploring the discrepancy between ISEE observations and Tsyganenko's models identified by *Huang et al.* [1990, 1991], and it therefore concentrated on the data sets labeled MDSISEE and MDSIMP in Table 1. The later stages of our study used the full suite of modeling data sets.

2.2. *Observed $\langle B_z \rangle$ in the Near-Earth Plasma Sheet*

The first phase of our study analyzed ISEE and IMP data sets (MDSISEE and MDSIMP from Table 1) using the same selection criteria for the plasma sheet as those used by *Huang and Frank* [1992]. Selected points had to satisfy all three of the following conditions: (1) $-10\ R_E \geq x_{GSM} \geq -22\ R_E$, (2) $-10\ R_E \leq y_{GSM} \leq 10\ R_E$, and (3) $|B_x| < 5$ nT. *Huang and Frank* [1993] used trends in the AU and AL indices to bin their high resolution (4-s) ISEE data according to phases of the substorm; their data set covered the first 2 years of the ISEE mission. For each resulting bin, they computed average values of B_z and B_y in various subranges of x and y. A summary of their results is presented in Table 2, including average values $\langle B_z \rangle$ for each of their substorm phase conditions; the last row in Table 2 gives the "grand average" over all conditions.

Our modeling data sets represented ~0.5 R_E averages, corresponding to a time scale of 10–20 min and did not include high-resolution information on AU and AL which might have allowed comparison with each of Huang's classifications. Instead, we used ranges of the magnetospheric index *Kp* to generate subsets of the ISEE and IMP ($R < 17\ R_E$) observations. Those data sets were used to compute averages $\langle B_z \rangle$, listed in Table 3. It must be noted that the ISEE modeling data set included data from a 4-year period (see MDSISEE row in Table 1) and thus was not simply an averaged version of the ISEE data used by Huang and collaborators.

Several interesting features are readily apparent by comparing Tables 2 and 3. First of all it should be noted that the overall average $\langle B_z \rangle$ observed by ISEE fits the one measured by IMP spacecraft (columns 2 and 3 in Table 3). Table 3 also makes evident the sparseness of IMP data points in the plasma sheet, cited earlier as one reason for the low $\langle B_z \rangle$ predicted by T87 and T89. Because of the flaring of the tail field lines, B_z tends to decrease (and ultimately to reverse its sign) with increasing z distance from the middle of the sheet; since most IMP tail data have larger values of $|z|$, their $\langle B_z \rangle$ is relatively small and that may have biased the models. Direct comparison within the different *Kp* levels is not possible since we lack a sufficient number of points for reliable statistics. More striking is the agreement between the two distinct ISEE data sets; namely the 4-s resolution set used by Huang et al. and the ~0.5 R_E set which we employed. One final observation, present in all sets and consistent with earlier model studies [*Tsyganenko and Usmanov*, 1982; *Tsyganenko*, 1987*a*, *b*, 1989], is the tendency toward higher $\langle B_z \rangle$ averages at higher magnetic activity, that is, the onset and recovery conditions in Table 2 and the highest *Kp* levels in Table 3.

2.3. *Tail $\langle B_z \rangle$ Predicted From Global Empirical Models*

To compare magnetic field models to the observations described above, the fields predicted by T87 and T89 at the spatial positions of the magnetic field observations were computed. The last column in Table 2 lists the average B_z

TABLE 2. Average $\langle B_z \rangle$ Values Computed by *Huang et al.* [1992] From ISEE Data (4-s Resolution) and From the T89*a* Model

Substorm Phase [*Huang et al.*, 1992]	$\langle B_z \rangle$ From ISEE 4-s Data	$\langle B_z \rangle$ From T89*a*
Quiet	4.65 (4,402)	3.24 (113)
Growth of expansive phase	6.57 (3,997)	2.98 (36)
Recovery of expansive phase	6.93 (2,300)	3.27 (37)
Multiple onset substorms	8.13 (2,648)	1.49 (24)
Growth of driven system	6.80 (3,820)	3.06 (134)
Recovery of driven system	7.93 (8,477)	2.80 (384)
Steady driven system	5.11 (13,507)	3.59 (181)
Total	6.29 (39,151)	3.04 (909)

Data were selected so that $-10\ R_E > x > -22\ R_E$, $|y| < 10\ R_E$, and $|B_x| < 5\ nT$. The number in parenthesis following the average indicates how many data points contributed to the determination of $\langle B_z \rangle$.

TABLE 3. Average $\langle B_z \rangle$ Values Computed From ISEE Data (Data Set MDSISEE With ~0.5 R_E Resolution), IMP: $R < 17$ R_E Data (Data Set MDSIMP With ~0.5 R_E Resolution), T87*b* and T89*a* Models (Derived From IMP/HEOS Data), and T87W*c* Models (Derived From ISEE Observations)

Kp Level	$\langle B_z \rangle$ ISEE Data	$\langle B_z \rangle$ IMP Data	$\langle B_z \rangle$ T87*b*, From IMP-HEOS Data	$\langle B_z \rangle$ T89*a* From IMP-HEOS Data	$\langle B_z \rangle$ T87 W*c* From ISEE Data
[0, 0^+]	4.89 (17)	5.80 (8)	3.69 (22)	3.21 (33)	5.70 (20)
[1^-, 1]	4.51 (64)	4.76 (15)	3.57 (70)	2.90 (91)	5.71 (68)
[1^+, 2^-]	5.04 (52)	4.38 (9)	3.61 (40)	3.18 (60)	5.70 (44)
[2, 2^+]	4.52 (55)	5.41 (4)	3.80 (75)	2.50 (88)	6.39 (56)
[3^-, 3, 3^+]	5.69 (58)	8.55 (10)	3.82 (52)	2.75 (66)	6.91 (48)
[4^-, 4, 4^+]	8.03 (28)	3.36 (1)	7.27 (16)	3.64 (41)	7.43 (18)
[5^-, 5]	6.31 (18)	···	10.48 (11)	5.68 (19)	8.69 (16)
$\geq 5^+$	10.74 (20)	15.01 (1)	17.72 (5)	5.69 (13)	14.44 (10)
Total	5.66 (312)	5.89 (48)	4.40 (291)	3.15 (411)	6.64 (280)

As in Table 2, the number in parenthesis indicate how many data points contributed to the determination of $\langle B_z \rangle$, and the selection criterion was $-10\ R_E > x > -22\ R_E$, $|y| < 10\ R_E$, and $|B_x| < 5$ nT.

values obtained in this manner by Huang et al. using the T89*a* model and a subset of the ISEE positions from their high-resolution data set. Comparison with the second column in Table 2 reveals the factor of 2 discrepancy in $\langle B_z \rangle$ originally claimed by Huang and collaborators.

In a similar manner, we have taken the average spacecraft positions from the MDSISEE data set, computed their predicted field according to the T87*b* and T89*a* models and listed the results respectively, in columns 4 and 5 of Table 3. It is readily apparent that $\langle B_z \rangle$ values predicted by T87*b* are much closer to the ISEE (and IMP) observations than those of T89*a*. However, both T89*a* and T87*b* underestimate $\langle B_z \rangle$ in the region, with T89*a* yielding ~50–55% of the observed $\langle B_z \rangle$ and T87*b* giving ~80%.

Our ~0.5 R_E observations reveal agreement between $\langle B_z \rangle$ values from IMP and ISEE in the near-Earth neutral sheet; furthermore, the ISEE averages corresponding to 10- to 20-min resolution yield $\langle B_z \rangle$ values comparable with those obtained by Huang and collaborators from the 4-s resolution data. The consistency between the various $\langle B_z \rangle$ computations coupled with the low values of $\langle B_z \rangle$ predicted by the T87*b* and T89*a* models suggest that new sets of model coefficients are necessary to accurately reproduce $\langle B_z \rangle$ in the near-Earth neutral sheet region.

3. Equatorial $\langle B_z \rangle$ From New Data-Based Models

A key feature of the ISEE orbits, in contrast to those of the IMP and HEOS spacecraft from which the original T87 and T89 models were derived, is their much better coverage of the near-Earth, equatorial plasma sheet region. Figure 1 illustrates the location of all ~0.5 R_E averages composing the MDSISEE data set; projected onto the noon-midnight plane. The orthogonal projection onto the equatorial plane (not shown) reveals uniform coverage in the dawn-dusk direction. The corresponding projection for the MDSIMP data set appears in Figure 2; the sparse coverage of the central plasma sheet region is partially responsible for the inability of IMP/HEOS-based models to properly reproduce the $\langle B_z \rangle$ behavior.

3.1. *Data-Based Global Models*

In order to test our conjecture that poor sampling near the neutral sheet contributed to the low $\langle B_z \rangle$ values, we derived new models based on the ISEE observations. A modified version, T87W, of the T87 scheme, incorporating tail warping effects [*Peredo and Stern*, 1991*b*], was used to derive ISEE-based models. Optimum values for the model coefficients were derived by nonlinear least squares (see Appendix B), and the new models, hereafter labeled T87W*c*, were used to predict $\langle B_z \rangle$ values as listed in the last column of Table 3. Comparison with other columns in Table 3 reveal that B_z averages predicted by the (ISEE-based) T87W*c* models are much closer to those observed. Warped T87W*b* models based on IMP/HEOS data produce a total average of 4.56 nT, whereas T87W*c* based on ISEE data yields 6.64 nT, in agreement with our stipulation that better coverage of the neutral sheet region by the ISEE spacecraft produces models with higher values of $\langle B_z \rangle$. Similar efforts to fit T89 models to the ISEE data set and to the combined IMP/HEOS/ISEE data sets produced B_z averages larger than the original T89, but still smaller than what the observations suggest [*Tsyganenko et al.*, 1992; *Stern and Tsyganenko*, 1992]. This may be an indication that the representation of the tail current system implied by T89 restricts the resulting values of $\langle B_z \rangle$. The relative smallness of $\langle B_z \rangle$ predicted in the tail by T89*a* is also underscored by the occurrence in the T89*a* tail of regions of negative (reversed) B_z, as noted by *Tsyganenko* [1989] and in more detail by *Donovan et al.* [1992].

As indicated before, the T87W*c* models exhibit less tailward stretching than the original T87 models. The stretching in a given model depends on both B_z and B_x; however, since B_x varies slowly down the tail, and differences in B_x between models are much less pronounced that those between B_z, we find a marked difference in the tailward stretching for B_z differences of just a couple of nanoTeslas. Figure 3 illustrates the strong dependence of the stretching on B_z for a moderate activity configuration with $Kp = 3^-$, 3, 3^+, for zero tilt ψ. The top half of the plot shows the equatorial plane for the T87*b* or T87W*b* (the two are the same if $\psi = 0$) model, while the bottom half shows the corresponding plane for the T87W*c* model. In each case the solid lines show the equatorial footprint of lines of constant magnetic latitude (67°, 67.5°, ···, 69.5°), while the dashed lines correspond to the mapping of lines of constant magnetic local time (2, 4, 6 for T87*b* and 18, 20, 22 for T87W*c*).

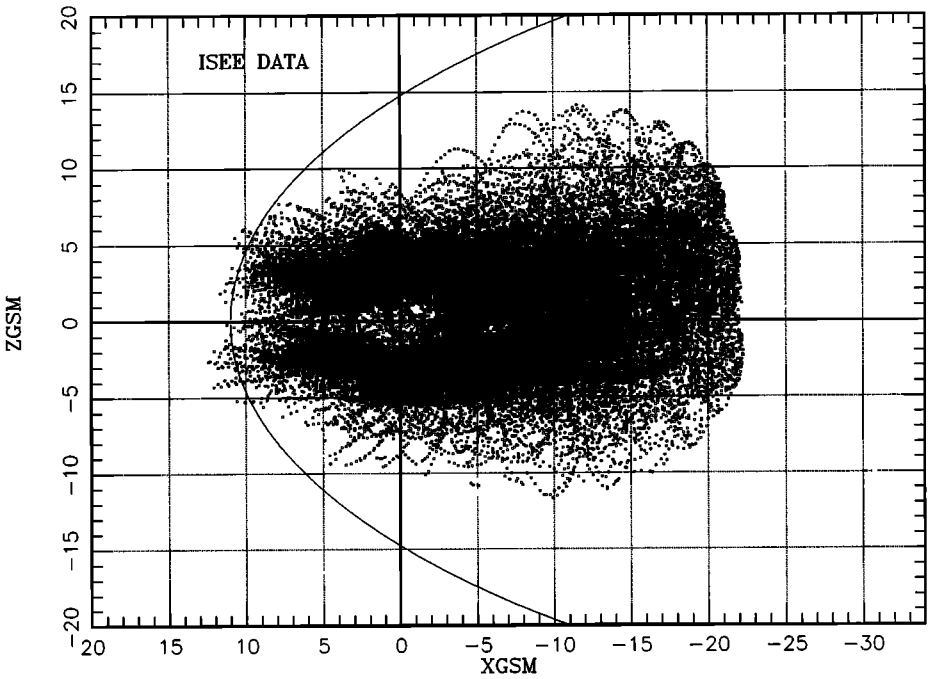

Fig. 1. Location of magnetic field averages from the ISEE spacecraft, corresponding to the set labeled MDSISEE in Table 1, projected onto the noon-midnight plane.

Two key points are readily apparent. It is clear that T87*b* is more stretched than the new T87W*c* model beyond $x_{GSM} \sim 15\ R_E$; furthermore, we find that the converse is true earthward of 15 R_E. Therefore we conclude that the increased values of $\langle B_z \rangle$ in T87W*c* arise from increased magnetic flux, relative to that in T87*b*, in the 10–20 R_E region; most of this flux has come from the tail, but a fraction has also been pulled from the region earthward of 10 R_E.

In the process of fitting the models to data it was realized that the accuracy of models in the near-Earth tail region was primarily determined not by the relatively small discrepancies in averaged $\langle B_z \rangle$ but rather by the huge scatter among the baselines of the observations. Figure 4 shows all observed values of $\langle B_z \rangle$ from ISEE (from the modeling data set MDSISEE), satisfying (1) $Kp \leq 2^+$, (2) $|y_{GSM}| < 10\ R_E$, (3) $|\Delta z| < 2\ R_E$, (4) $x_{GSM} \leq -10\ R_E$, and (5) $|B_H| < 5$ nT,

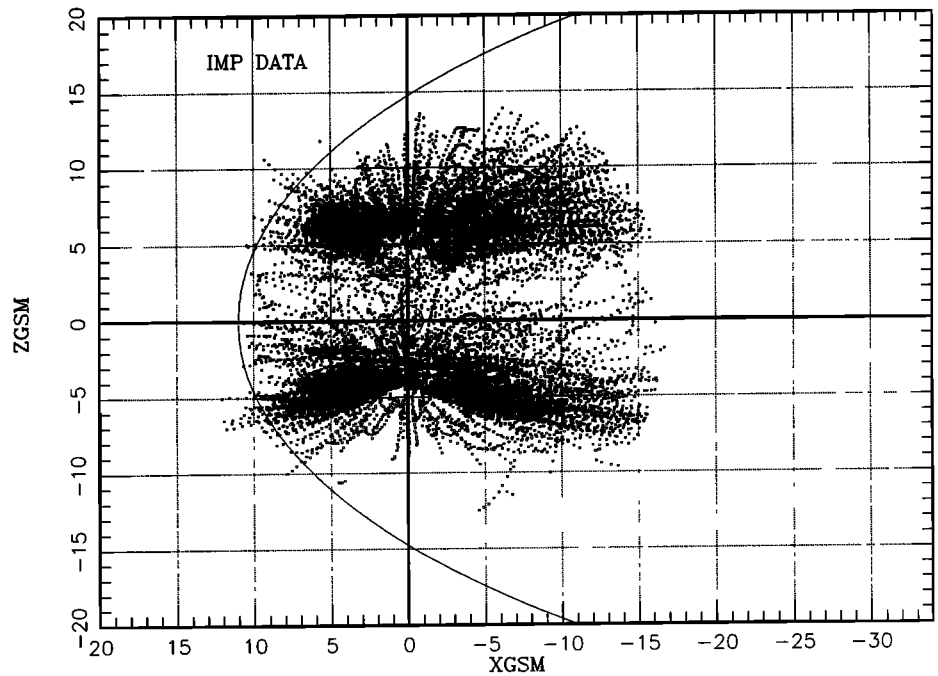

Fig. 2. Location of magnetic field averages from IMP spacecraft, corresponding to the set labeled MDSIMP in Table 1, projected onto the noon-midnight plane.

where Δz represents the difference in z between the observation and the model's tail current sheet, and $B_H = [B_x^2 + B_y^2]^{1/2}$ is the horizontal component of the magnetic field. For comparison, the solid line in Figure 4 shows the B_z distribution predicted by the T89*a* model. Similar figures (not shown) for different magnetic activity ranges or different data sets reveal a scatter in $\langle B_z \rangle$ values comparable to the one shown in Figure 4. It is clear that until we trace the source of this variation and incorporate it in our models, predicted values of $\langle B_z \rangle$ will continue to have enormous error bars.

We conclude that T87W*c* gives a better representation than T87*b* or T89*a* in the 10–20 R_E tail region. In a separate study [*Tsyganenko*, 1989], it was shown that the T89 scheme yields a better representation of the magnetic field in the geosynchronous region than the one resulting from T87 since its tail model field includes a B_y component. Even as modified, T87W lacks a dawn-dusk component of the model tail field, needed to model tail flaring, and like T87, is inferior to T89 in the geosynchronous region. Computer codes and sets of coefficients for all the models (see Appendix A for a detailed list of available models), including new models based on the combined IMP/HEOS/ISEE data set, may be obtained from the authors; we recommend that the new coefficients be used, rather than the ones originally published [*Tsyganenko*, 1987*a*, *b*, 1989], and that the tail-warping option [*Peredo and Stern*, 1991*a*, *b*] be used as an improvement to the T87 model.

3.2. *A Local Tail Model*

Global models such as T87 or T89 are inherently limited in representing the tail's $\langle B_z \rangle$ because their parameters often represent a compromise in matching magnetic field data from

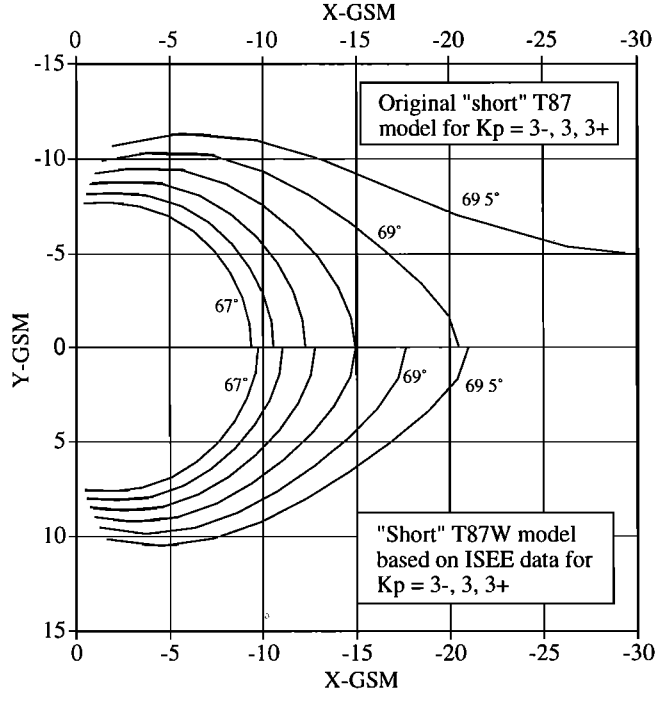

Fig. 3. Equatorial mapping of lines of constant magnetic latitude (solid) and constant magnetic local time (dashed) using the T87*b* (top) and T87W*c* (bottom) models for moderate activity conditions ($Kp = 3^-, 3, 3^+$), and zero tilt angle.

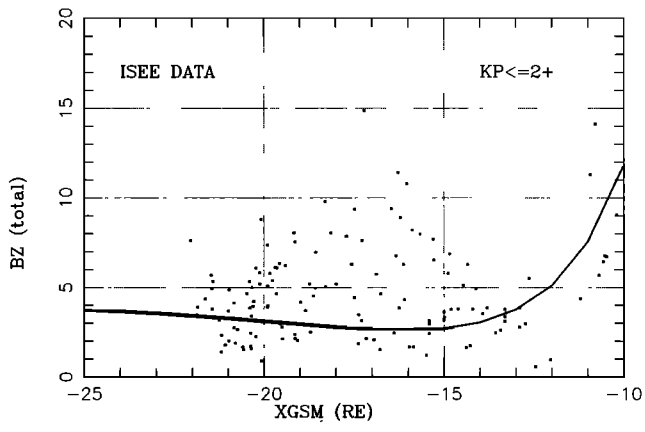

Fig. 4. Distribution of the north-south magnetic field component B_z observed by ISEE as a function of distance down the tail. Data points are restricted to satisfy the conditions: $Kp \leq 2^+$, $|\Delta z| < 2\ R_E$, $|Y_{GSM}| < 10\ R_E$, and $|B_H| < 5$ nT. For comparison, the solid line illustrates the corresponding B_z predicted by the T89*a* model.

different regions of the magnetosphere. The need for these parameters to match observations globally may compromise the model's accuracy in the near-Earth tail. In addition to the mentioned discrepancy with the measured $\langle B_z \rangle$ values, such global fitting has produced unrealistic reversals of the model B_z at $x_{GSM} \sim -15\ R_E$ emerging at large values of tilt angle [*Donovan et al.*, 1992]. A local model provides a useful alternative for studying local behavior such as particle motion, but is not appropriate for field line mappings where one needs to model the entire region between the polar ionosphere and the equatorial magnetosphere. In this section, instead of refining the global tail models, we only model a limited region of the magnetotail and use the spacecraft measurements made there to derive the parameters of a flexible local magnetic field model. The relatively smooth variation of the tail field along the x and y directions makes it possible to model the corresponding vector potential by simple analytical expressions which can be easily modified to account for tilt-related warping effects.

We have assumed that the extent of the modeling region was sufficiently small for the variation of the tail field components along the x_{GSM} axis to be approximated by two or three exponential terms. The B_x component varies in the north-south direction like a step function, it rapidly changes sign on crossing the current sheet and is nearly constant outside of the reversal region. The dawn-dusk variation of the field components can be approximated by a linear dependence (for B_y) or a quadratic one (for B_x and B_z) on y_{GSM}. A similar approach was employed by *Tsyganenko* [1987*b*] for local modeling of the magnetotail magnetic field. However, the earlier model was based on direct expansions of the magnetic field components produced by a planar current sheet and thus did not allow for the equatorial surface to be warped. In the present work a more general case is addressed. Instead of the field components, we now start from the vector potential **A** for the planar current sheet and then impose modifications which enable the model to simulate variations of the current sheet thickness along the dawn-dusk and Sun-Earth directions, as well as the warping of the sheet in response to seasonal and diurnal variation of the geodipole tilt angle ψ. No restriction is placed on $\nabla \cdot \mathbf{A}$.

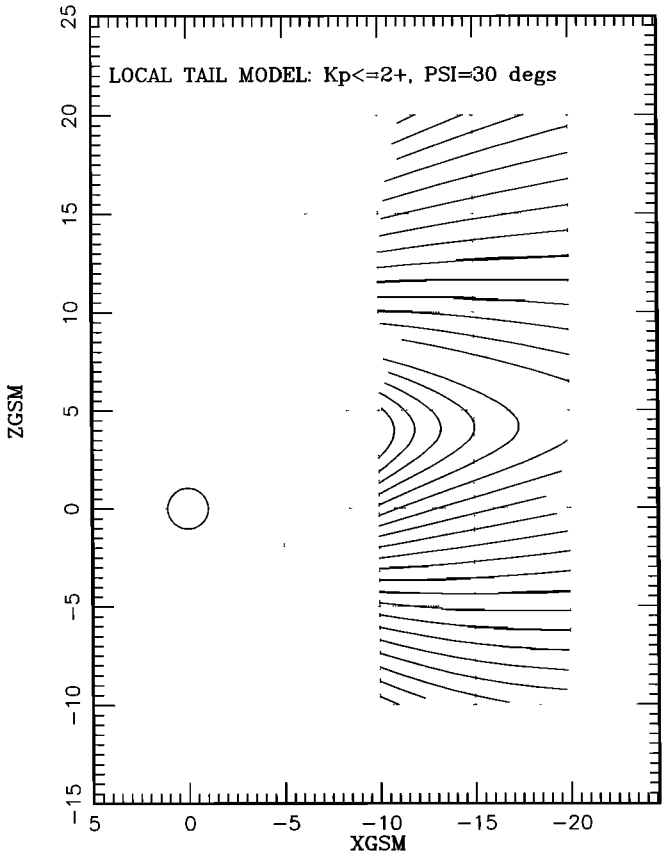

Fig. 5. Average field line structure in the near-tail region according to the local model for $Kp \leq 2^+$ and tilt angle $\psi = 30°$.

To obtain a flexible representation for the three components of the magnetic field, it is enough to assume a vector potential A with no z component, reflecting the predominance of the x and y components of the electric current density in the equatorial tail current sheet. The potential A is completely determined by its A_x and A_y components; using the known basic properties of the tail magnetic field, including symmetry considerations, they are expanded as follows:

$$\begin{aligned} A_x &= y[a_1 + a_2\zeta + a_3\zeta^2 + (a_4\zeta + a_5\zeta^2)\exp(x/\Delta x_1) \\ &\quad + (a_6\zeta + a_7\zeta^2)\exp(x/\Delta x_2)] \\ A_y &= a_8\zeta + a_9\zeta^2 + (a_{10} + a_{11}\zeta + a_{12}\zeta^2)\exp(x/\Delta x_1) \\ &\quad + (a_{13} + a_{14}\zeta + a_{15}\zeta^2)\exp(x/\Delta x_2) \\ &\quad + y^2[a_{16}\zeta + a_{17}\zeta^2 \\ &\quad + (a_{18} + a_{19}\zeta + a_{20}\zeta^2)\exp(x/\Delta x_1) \\ &\quad + (a_{21} + a_{22}\zeta + a_{23}\zeta^2)\exp(x/\Delta x_2)] \\ &\quad + a_{24}\psi z \exp(x/\Delta x_3) \end{aligned} \tag{1}$$

where the variable ζ is defined by the relations

$$\begin{aligned} \zeta &= [z_r^2 + d^2(x, y)]^{1/2} \\ z_r &= z - z_s(y, \psi) \end{aligned} \tag{2}$$

The function ζ tends to z_r at large distances and to a constant d near the central surface of the model current sheet, whose shape is given by $z = z_s(y, \psi)$. Therefore, the terms in (1) linear with respect to ζ provide a nearly uniform field in the tail lobes, while at small z_r, equation (1) yields a spread-out current sheet. The term containing the dipole tilt angle ψ allows for possible asymmetry between the northern and southern tail lobes due to the geodipole tilt.

For the function $z_s(y, \psi)$ defining the shape of the model current sheet we use a form similar to $z_s(x, y, \psi)$ proposed by *Tsyganenko* [1989]; the only difference is that no dependence on the x coordinate is assumed, since the modeling region in this study is tailward of $x_{GSM} = -10\,R_E$, and hence no major curvature along the x axis is expected. The explicit form of the function z_s given below uses the GSM coordinate system (rather than SM used in the formula (11) of *Tsyganenko* [1989] and is given below:

$$z_s(y, \psi) = \left[R_H - \frac{Gy^4}{y^4 + L_y^4}\right] \sin\psi \tag{3}$$

The parameter R_H (the "hinging distance") defines the amplitude of north-south excursions of the midnight part of the current sheet, while G and L_y define the degree and spatial extension of the sheet warping in the y-z plane; all three quantities are free model parameters fitted to the data, which allows one to study the shape of the current sheet and its dependence on solar wind conditions. A somewhat different approximation to z_s is given in (A11) of the appendix. The half-thickness of the current sheet is approximated by

TABLE 4. Best Fit Parameters for the Local Model of the Near Magnetotail

K_p	[0, 2⁺]	[3⁻, 3⁺]	[4⁻, 9⁺]
a_1	−4.700	−0.9349	−6.555
a_2	0.548	−0.1143	0.354
a_3	−50.65	−115.3	−96.23
a_4	−11.12	−9.984	−14.13
a_5	−0.025	−0.00196	−0.03014
a_6	1.800	3.254	2.416
a_7	0.316	0.2759	0.5145
a_8	−8.267	−8.895	−16.22
a_9	−0.239	−0.374	−0.2992
a_{10}	2332.0	127.7	2937.9
a_{11}	−518.2	−391.4	−713.3
a_{12}	22.08	21.97	44.08
a_{13}	118.5	528.7	150.7
a_{14}	−141.9	−201.8	−189.1
a_{15}	3.229	5.373	3.866
a_{16}	−0.0556	−0.1318	−0.1567
a_{17}	0.00132	0.00398	0.00614
a_{18}	−28.59	−8.659	8.090
a_{19}	3.604	−0.6583	−3.501
a_{20}	−0.1072	0.0733	0.2013
a_{21}	−2.979	−5.404	−5.365
a_{22}	0.3236	0.7866	0.8404
a_{23}	−0.00869	−0.029	−0.0318
a_{24}	0.7757	3.702	2.200
R_H	7.90	7.02	7.17
G	21.05	34.03	56.18
L_y	16.50	19.00	22.59
d_0	2.01	1.72	1.46
d_1	12.83	12.46	10.29
d_2	0.17	0.20	0.17
Δ_{x1}	2.23	2.08	2.08
Δ_{x2}	9.23	8.48	8.26
Δ_{x3}	−12.91	−26.77	−15.40

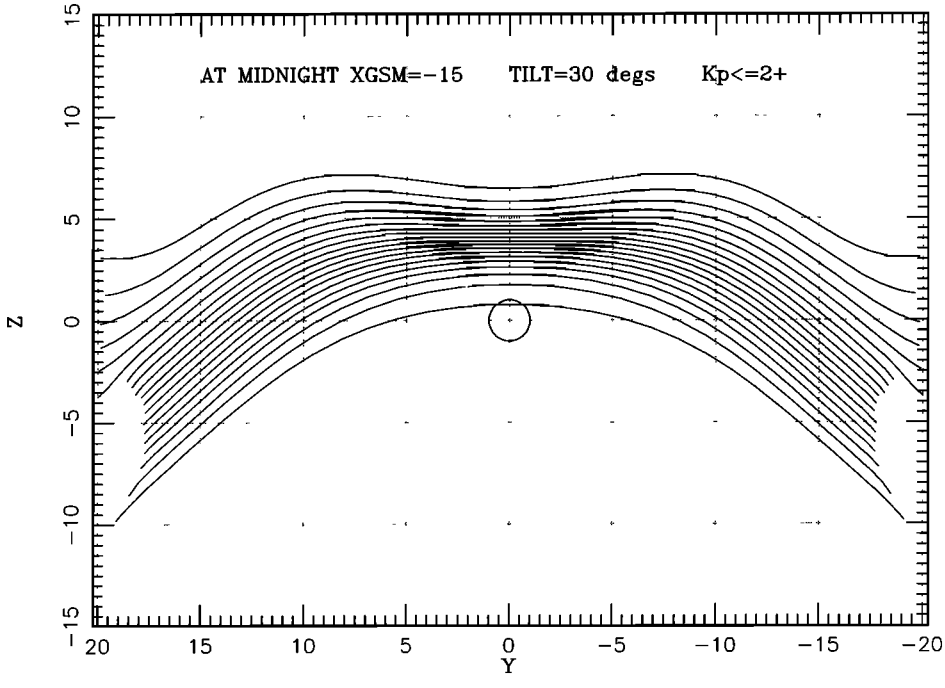

Fig. 6. Electric current streamlines crossing the midnight meridian at $x_{GSM} = -15\ R_E$ shown in the y-z projection. The line density is proportional to local values of the electric current density. The warping of the tail current sheet due to the geodipole tilt is clearly seen.

$$d(x, y) = d_0 + d_1\left(\frac{y}{20}\right)^2 + d_2\left(\frac{x + 15}{10}\right) \qquad (4)$$

It depends quadratically on y and linearly on x, with the coefficients d_0, d_1, and d_2 also considered as free parameters, nonlinear in the sense that they appear in the model in a nonlinear fashion in (2). In total, the present model contains 24 linear and 9 nonlinear parameters, and analytical expressions for the magnetic field components can be found from (1) in a straightforward way by calculating derivatives of the A components:

$$B_x = -\frac{\partial A_y}{\partial z},\ B_y = \frac{\partial A_x}{\partial z},\ B_z = \frac{\partial A_y}{\partial x} - \frac{\partial A_x}{\partial y} \qquad (5)$$

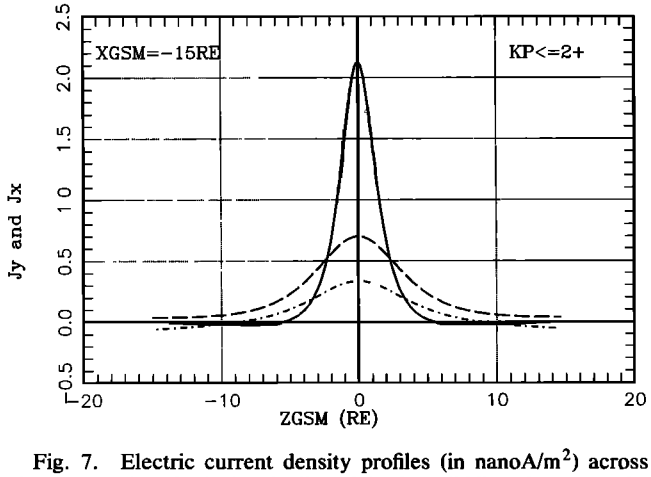

Fig. 7. Electric current density profiles (in nanoA/m^2) across the current sheet in the local tail model. The solid line gives j_y on the midnight meridian plane, while the dashed and dashed-dotted curves represent j_y and j_x, respectively, on the plane $y_{GSM} = 10\ R_E$.

The data sets for determination of the model parameters consisted of vector averages from the IMP-HEOS and ISEE data files from the interval $-20 < x_{GSM} < -10\ R_E$. Most of the data came from the ISEE data set. Figure 5 provides a graphic illustration of the average field line structure produced by the local model in the near magnetotail, in this case for quiet conditions ($Kp < 2^+$) and a tilted geodipole.

Table 4 lists the local tail model parameters for low, middle, and high disturbance levels. The midnight half-thickness of the current sheet d_o lies within the range 1.5–2.0 R_E and becomes smaller for larger values of Kp, while the parameter d_1 remains almost constant and corresponds to a rather significant increase of the current sheet half-thickness toward the tail flanks (to 4–5 R_E at $y = 10\ R_E$ and 7–9 R_E at $y = 15\ R_E$). The parameter d_2 is small, suggesting a near-constancy of the sheet thickness along the tail axis provided that the sheet thickness varies monotonically with x_{GSM} within the modeling region. The hinging distance R_H for all three cases lies in the narrow range 7.0–7.9 R_E, in good agreement with previous studies, and the warping effect defined by the parameters G and L_y has the expected sign and magnitude, as seen in Figure 6 which shows a family of electric current flow lines crossing the midnight meridian plane at $x_{GSM} = -15\ R_E$.

Figure 7 displays the north-south profiles of the electric current density across the current sheet at midnight and halfway to the dusk magnetopause. The lowest curve shows a significant positive x component of the j vector, as expected from earlier results indicating that electric current flow lines in the near-Earth plasma sheet are concave toward Earth [e.g., *Speiser and Ness*, 1967].

Let us apply the local model to the average B_z distribution in the equatorial magnetosphere. Figure 8 shows the midnight profiles of predicted equatorial $\langle B_z \rangle$ in the near-tail, for

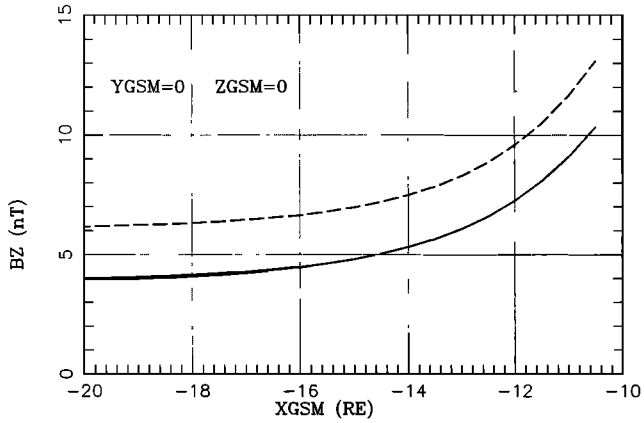

Fig. 8. North-south magnetic field component predicted by the local tail model for two levels of magnetic activity. The dashed line corresponds to $Kp \geq 4^-$, while the solid line satisfies $Kp \leq 2^+$.

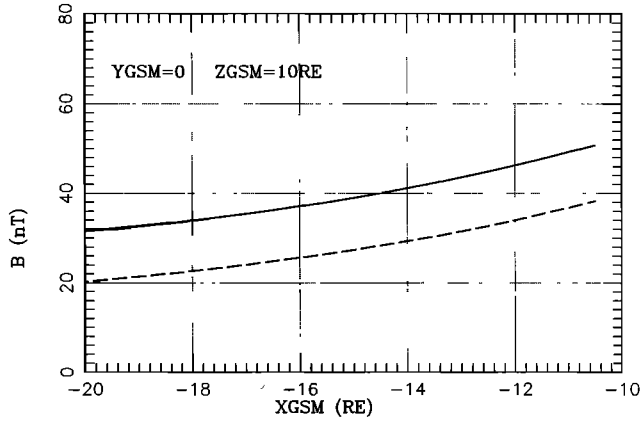

Fig. 10. Average effect of changes in the solar wind dynamic pressure on the net tail lobe magnetic field predicted by the local model. The solid line corresponds to high pressure values, $p_{dyn} > 2.60$ nPa, while the dashed line is for $p_{dyn} < 1.47$ nPa.

low and high Kp values. At least two features are conspicuous. First, larger predicted values of $\langle B_z \rangle$ go with higher Kp values in the whole range $-20 < x_{GSM} < -10\,R_E$, in line with the earlier result obtained there by the T87 and T89 models and with the $\langle B_z \rangle$ values computed directly from the data (see section 2.2 above). Studies using statistics [*Fairfield et al.*, 1987] and models [*Tsyganenko*, 1987*a*, 1989] have shown that closer to the Earth the opposite effect is observed: larger Kp values correspond to smaller $\langle B_z \rangle$, suggesting that, on average, the largest nightside electric current associated with magnetospheric disturbances flows in the vicinity of $x_{GSM} \sim -10\,R_E$. Second, the present values of $\langle B_z \rangle$ exceed those predicted from T89 by a few nanoTesla, corroborating the results of *Huang et al.* [1991] and *Rostoker and Skone* [1993]. Compare, for instance, the lower curve with Figure 4.

Figure 9 shows the variation of the predicted equatorial $\langle B_z \rangle$ in the y direction (dawn-dusk). In agreement with the statistical result of *Fairfield* [1986], a significant increase of $\langle B_z \rangle$ occurs toward the tail flanks. Figure 10 illustrates the average response of the net tail lobe magnetic field to changes in the solar wind dynamic pressure. In this case, the model parameters were computed by using data points selected for two intervals of P_{dyn}: a low-pressure data set with $P_{dyn} < 1.47$ nPa and a high pressure one satisfying $P_{dyn} > 2.60$ nPa. Average values of P_{dyn} for the two sets were 1.03 and 4.80 nPa, respectively. As expected, larger pressure corresponds to stronger lobe fields.

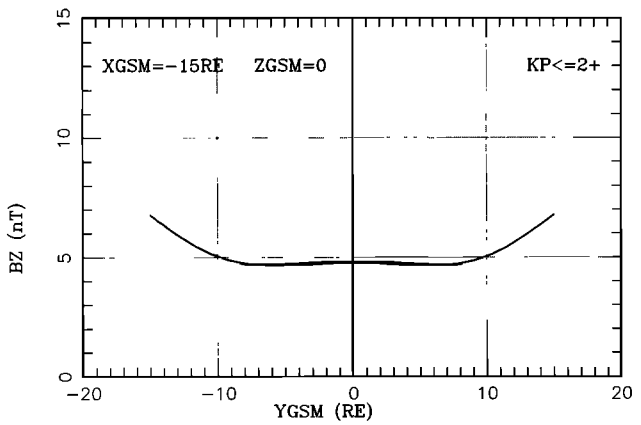

Fig. 9. Dawn-dusk variation of the equatorial B_z predicted by the local tail model.

4. SUMMARY AND CONCLUSIONS

Both the T87*b* and T89*a* models are excessively stretched in the region $-10\,R_E > x_{GSM} > -22\,R_E$. Comparison between them and observations confirm a study by *Huang et al.* [1991, 1993] and reveal that both underestimate $\langle B_z \rangle$ in the near-Earth tail region, with T89*a* yielding ~50–55% of the observed $\langle B_z \rangle$ while T87*b* gives ~80%. A modified T87W*c* model (incorporating plasma sheet warping) fitted to the ISEE data alone yields $\langle B_z \rangle$ values in good agreement with the ISEE data (and with the study by Huang and collaborators). A local tail model has been developed which provides a better representation of the $\langle B_z \rangle$ distribution in the tail, but is not suitable for tracing field lines to and from the ionosphere. The inadequate representation of $\langle B_z \rangle$ in earlier models arose, in part, because the IMP/HEOS data sets, on which T87*b* and T89*a* were based, had relatively poor coverage of the equatorial region. The dominant source of discrepancy between observed values of $\langle B_z \rangle$ and those predicted by models is, however, the large scatter among the average baselines of the magnetic field observations. Until modelers trace the source of this variability and take it into account, values of $\langle B_z \rangle$ predicted by any model, global or local, will continue to have enormous error bars.

We recommend caution when using either T87, its warped variant T87W or T89. While Tsyganenko's previous work suggest that models using the T89 scheme represent the geosynchronous region better than those using the T87 formulation, this study suggests that T87 models, and in particular their modified versions T87W, better represent the nightside equatorial region between 10 and 20 R_E. Clearly, models are only as good as the data on which they are based; the addition of the ISEE data set to the modeling database has certainly influenced the properties of the models. Computer codes for all the models (in FORTRAN), including those with new coefficients, computed from the combined IMP/HEOS/ISEE data set, are available from the authors, and these versions of the model should be used in place of the original T87 and T89 models (requests may be addressed

TABLE 5. Catalog of Existing Magnetospheric Models

Model Designation	Based on Dat a From	Activity Levels and Criterion	Tailward Range of Validity	Reference and/or Comments
T87*a*	IMP-HEOS	6 by K_p	70 R_E	Original (Long) T87 model [*Tsyganenko*, 1987]
T87*b*	IMP-HEOS	8 by K_p	30 R_E	Original (Short) T87 model [*Tsyganenko*, 1987]
T87W*a*	IMP-HEOS	6 by K_p	70 R_E	Warped variation of (Long) T87 using *Gosling et al.* [1986] formula [*Peredo and Stern*, 1991*b*]
T87W*b*	IMP-HEOS	8 by K_p	30 R_E	Warped variation of (Short) T87 using *Gosling et al.* [1986] formula [*Peredo and Stern*, 1991*b*]
T87WS*a*	IMP-HEOS	6 by K_p	70 R_E	Stern variation of T87W*a* with current free lobes [*Stern*, 1990]
T87WS*b*	IMP-HEOS	8 by K_p	30 R_E	Stern variation of T87W*b* with current free lobes [*Stern*, 1990]
T87W*c*	ISEE	8 by K_p	22 R_E	Warped variation of (Short) T87 based on ISEE data [*Peredo and Stern*, 1991*a*]
T87W*d*	IMP-HEOS-ISEE	6 by K_p	70 R_E	T87 with warping effects incorporated self-consistently (using (3))
T87W*e*	IMP-HEOS-ISEE	12 by p_{sw} and IMF-B_z	30 R_E	Self-consistently warped T87 organized by solar wind and IMF conditions [*Peredo et al.*, 1992]
T89*a*	IMP-HEOS	6 by K_p	70 R_E	Original T89 model [*Tsyganenko*, 1989]
T89*b*	IMP-HEOS	6 by AE	70 R_E	Variant of T89 organized by AE
T89*c*	IMP-HEOS-ISEE	7 by K_p	70 R_E	Revised T89 based on expanded data set

to LEPVAX::YS2NT (until February 1994), LEPVAX::U5DPS or LEPVAX::XR2MP). For studies limited to the tail region, the local model is the preferred field representation.

APPENDIX A: EXISTING MAGNETIC FIELD MODELS

The Tsyganenko magnetic field models [*Tsyganenko*, 1987*a*, 1989] are commonly identified as T87 and T89. These designations are however insufficient to properly identify the particular model used. The modeling data base used to derive these models has doubled in size since the original models were derived. New models have been derived using the enhanced data base and several variants of the T87 model have been constructed. Such proliferation of models makes more apparent the deficiency of the designations T87 and T89. We present a revised nomenclature scheme that clearly identifies each model.

Our proposed nomenclature uses capital letters to designate mathematical schemes for representing the field, and lower case letters to distinguish different sets of model coefficients. The mathematical formulations thus include the original T87, its warped variant T87W [*Peredo and Stern*, 1991*b*], a version, T87S, with current-free tail lobes proposed by *Stern* [1990], a combined warped and current-free lobe variant T87WS, as well as T89. Each scheme for representing the magnetic field may have more than one set of coefficients corresponding to different databases used to generate the models or to different schemes of binning the data, for example, by *Kp* or by solar wind properties.

Table 5 provides a list of currently available models along with information on their domain of validity, levels of magnetic and/or solar wind activity and source of the data bases used to generate them. The new models, T87W*d*, T87W*e* and T89*c*, are based on the expanded IMP-HEOS-ISEE data base, and are clearly superior to models based on IMP-HEOS data alone. It is, however, impossible to single out one model as best suited for all purposes. *Tsyganenko* [1989] has shown that T89 fits the geosynchronous **B** better than T87 (and presumably T87W). The present study on the other hand suggests that, in the near-tail region, T87W yields a better representation of B_z and produces a dramatic difference in the tailward stretching of the field lines. We therefore recommend using T87W*d*, T87W*e* and T89*c* with the understanding that significant differences exist between their predicted fields.

APPENDIX B: DERIVATION OF MODELS BY NONLINEAR LEAST SQUARES FITTING

Levenberg-Marquardt Method for Nonlinear Least Squares Fitting

The formal derivation of magnetic field models from large sets of observations is based on the method of least squares fitting (see for example, chapter 11 of *Bevington* [1969] or chapter 14 of *Press et al.* [1989]. The goal is to fit a large number of observations of the magnetic field **B** at locations **x** = [x, y, z, tilt] in four-dimensional position+tilt space, to a representation $\mathbf{B}^{\mathrm{mod}}(\mathbf{x}, \mathbf{a})$ containing M free parameters, denoted by the vector $\mathbf{a} = [a_1, a_2, a_3, \cdots a_M]$. This approach, used to derive T87 and T89, fits the model to observed field vectors alone; future models are likely to rely on other data as well, for example, boundary crossings of the magnetopause [*Sibeck et al.*, 1991].

The fitting process formally seeks to minimize the merit function χ^2 (**a**), that is, the goal is to satisfy

$$\frac{\partial \chi^2}{\partial a_k} = 0, \qquad (k = 1, \cdots, M) \tag{B1}$$

where

$$\chi^2 = \sum_{i=1}^{N} \left[\frac{\mathbf{B}_i^{\mathrm{obs}} - \mathbf{B}^{\mathrm{mod}}(\mathbf{x}_i; a)}{w_i} \right]^2 \tag{B2}$$

measures the deviation between N observations $\mathbf{B}_i^{\mathrm{obs}}$, i = 1, $\cdots$, N and the corresponding model predictions $\mathbf{B}^{\mathrm{mod}}(\mathbf{x}_i$, **a**). Individual weights w_i may be assigned to the observations to emphasize data points with particular characteris-

TABLE 6. Distribution of the Difference Between Resulting T87W*c* Models and ISEE Observations for Different Magnetic Activity Levels

K_p Range	0, 0^+	1^-, 1	1^+, 2^-	2, 2^+	3^-, 3, 3^+	4^-,4, 4^+	5^-, 5	$K \geq 5^+$	Normal Distribution
N	1877	4770	5590	6075	6938	3553	1273	1299	...
σ	9.68	11.28	12.91	14.95	17.54	22.77	22.98	36.36	...
				Percentage					
Fraction within									
0–σ	76.079	84.088	81.216	79.012	79.519	73.825	84.368	66.898	68.268
σ–2σ	20.192	13.187	15.403	17.531	16.720	20.236	12.647	20.708	27.182
2σ–3σ	2.664	1.866	2.719	2.963	2.940	3.997	2.514	6.543	4.280
3σ–4σ	0.533	0.587	0.537	0.329	0.605	1.464	0.393	3.618	0.264
4σ–5σ	0.320	0.147	0.054	0.132	0.115	0.310	0.079	1.309	0.006
5σ–6σ	0.107	0.084	0.054	0.016	0.072	0.084	0.	0.231	
$\geq 6\sigma$	0.107	0.042	0.018	0.016	0.029	0.084	0	0.693	
One-Count Level	0.053	0.021	0.018	0.016	0.014	0.028	0.079	0.077	

Entries identify the fraction of data points for which the difference $[B_i^{obs} - B^{mod}(x_{i,a})]$ is less than n times the model's standard deviation. The final column lists the corresponding fractions for a normal distribution.

tics. Equivalently, we may speak of minimizing the root mean squared deviation $\sigma = [\chi^2/N]^{1/2}$.

If $\mathbf{B}^{mod}$ depends linearly on the parameters a_k, (B1) gives a system of linear equations which are readily solved; this is the simplest and most common case of least squares fitting. If, however, the dependence is nonlinear, we must search for the minimum of χ^2 in the multidimensional space spanned by the parameters a_k. The Levenberg-Marquardt method [*Marquardt*, 1963] accomplishes this minimization through an elegant interplay between two schemes. Far from the minimum, the steepest descent method is used, switching to the inverse Hessian method as the minimum is approached. The two methods rest on the assumption that close to the minimum, χ^2 may be expressed as a quadratic form:

$$\chi^2(\mathbf{a}) = \chi^2(\mathbf{a}_0) + \sum_k \left.\frac{\partial \chi^2}{\partial a_k}\right|_{\mathbf{a}_0} a_k + \frac{1}{2}\sum_{j,k} \left.\frac{\partial^2 \chi^2}{\partial a_j \partial a_k}\right|_{\mathbf{a}_0} a_j a_k$$

$$\equiv c - 2\beta \cdot \mathbf{a} + \mathbf{a} \cdot \alpha \cdot \mathbf{a} \tag{B3}$$

neglecting terms of cubic or higher order in the Taylor series expansion of χ^2 about $\mathbf{a}_0$; here β is a vector and α a matrix. Close to the minimum, where equation (B3) gives a good approximation to the merit function, the inverse Hessian method yields the minimizing solution with a single jump from the current trial parameters $\mathbf{a}_{current}$

$$\mathbf{a}_{min} = \mathbf{a}_{current} + 2\alpha^{-1}[-\nabla\chi^2(\mathbf{a}_{current})] \tag{B4}$$

Conversely, far from the minimum, (B3) gives a poor local approximation to χ^2 and the best course of action is to advance along the gradient; this is the steepest descent method. The trial solution is then advanced according to

$$\mathbf{a}_{next} = \mathbf{a}_{current} - \text{constant} \times \nabla\chi^2(\mathbf{a}_{current}) \tag{B5}$$

Following standard practice, we cast the problem in matrix notation and seek the correction term $\delta\mathbf{a}$, satisfying $\alpha \cdot \delta\mathbf{a} = \beta$, where in accordance to (B3) we have defined,

$$\alpha_{kl} = \frac{1}{2}\frac{\partial^2 \chi^2}{\partial a_k \partial a_l} \tag{B6}$$

$$\beta_k = -\frac{1}{2}\frac{\partial \chi^2}{\partial a_k} \tag{B7}$$

Substitution of (B2) in (B6) shows that the components α_{kl} depend on both the first and second derivatives of the fitting functions $\mathbf{B}^{mod}(\mathbf{x}_i, \mathbf{a})$ with respect to the parameters a_k. In practice, however, the second derivative terms are ignored since they have a numerically destabilizing effect (see, for example, section 14.4 of *Press et al.* [1989]). Accordingly, we replace (B6) with the definition

$$\alpha_{kl} = \sum_{i=1}^{N} \frac{1}{w_i^2}\left[\frac{\partial \mathbf{B}^{mod}(x_i, a)}{\partial a_k}\frac{\partial \mathbf{B}^{mod}(x_i, a)}{\partial a_l}\right] \tag{B8}$$

Marquardt's insight has been to combine the inverse-Hessian and steepest descent methods into a single formulation by defining a new matrix α':

$$\alpha'_{jk} \equiv \alpha_{jj}[1 + \lambda] \quad (j = k)$$
$$\alpha'_{jk} \equiv \alpha_{jk} \quad (j \neq k) \tag{B9}$$

where λ is a constant, related to the undetermined constant in (B5). Equations (B4) and (B5) are then combined into a single equation for the correction vector $\delta\mathbf{a}$

$$\sum_{l=1}^{M} \alpha'_{kl}\delta a_l = \beta_k \tag{B10}$$

For large λ, the matrix α' is forced into being diagonally dominated, and (B10) reduces to the steepest descent scheme, while in the limit of small λ, we recover the inverse-Hessian approach.

Given an initial guess for the set of fitted parameters $\mathbf{a}$, implementation of the Levenberg-Marquardt method proceeds according the following recipe: (1) evaluate the merit function $\chi^2(\mathbf{a})$, (2) select a modest value for λ, say $\lambda = 0.001$, (3) solve (B10) for the correction term $\delta\mathbf{a}$ and evaluate $\chi^2(\mathbf{a} + \delta\mathbf{a})$, (4) if the new solution is worse, that is, $\chi^2(\mathbf{a} + \delta\mathbf{a}) \geq \chi^2(\mathbf{a})$, increase λ by a factor 10 and go back to step (3); alternatively, if $\chi^2(\mathbf{a} + \delta\mathbf{a}) < \chi^2(\mathbf{a})$, decrease λ by a factor 10, update the trial solution $\mathbf{a} + \delta\mathbf{a} \rightarrow \mathbf{a}$ and go back to step (3).

TABLE 7. Coefficients for T87W*c* Model Based on ISEE Data

	$0, 0^+$	$1^-, 1$	$1^+, 2^-$	$2, 2^+$	$3^-, 3, 3^+$	$4^-, 4, 4^+$	$5^-, 5$	$K \geq 5^+$
N	1877	4770	5590	6075	6938	3553	1273	1299
σ	9.68	11.28	12.91	14.95	17.54	22.77	22.98	36.36
B_0	19.480186	19.751959	23.317072	21.644115	23.546949	28.455481	32.091736	33.068184
B_1	−270.3189	−140.1044	−292.7320	−162.0208	−358.8518	−161.2663	−186.4691	−329.9777
x_N	−3.694034	−2.431701	−4.266835	−2.656997	−2.827158	−2.971751	−2.829110	−2.983565
x_1	43.919872	27.469376	3.443168	6.698511	30.821966	3.199740	−0.452021	−3.604491
R_T	29.082855	28.899534	29.277739	28.337585	27.990709	28.669254	30.132742	65.599174
D	2.392427	2.048771	2.748451	.815448	.386922	.033619	.918309	3.001764
ΔY	15.593858	15.201653	2.136614	8.471653	2.147619	1.506317	0.588418	2.226160
B_{RC}	−26.11609	−29.23509	−37.92119	−41.15009	−50.09452	−52.31387	−75.72835	−117.39169
R_{RC}	6.215451	7.048045	6.013135	6.521522	6.475565	5.581587	4.559837	2.431780
Δ_{x1}	25.681391	22.900438	23.766304	23.133785	23.060505	20.100000	6.655788	8.173691
a_1	0.517116	0.759533	0.928245	.177661	.871147	2.597734	2.948882	3.446286
a_2	21.487164	26.147104	24.230762	31.938900	32.976105	34.836254	40.107021	64.580147
a_3	−0.035861	−0.063583	−0.049234	−0.071886	−0.055806	−0.028007	−0.105462	−0.221317
a_4	0.073878	0.107675	0.139419	0.103793	0.157304	0.021989	0.266315	−0.321763
c_1	18.687511	21.776712	23.075693	26.241322	30.668779	24.263546	22.419714	2.692634
c_2	−0.010028	−0.006266	−0.026208	−0.017921	−0.058540	−0.037486	−0.046148	0.082211
c_3	0.023742	0.006730	0.024905	0.015267	0.007703	−0.018758	−0.122931	0.021681
c_4	−0.059673	−0.346877	−0.099232	−0.574516	−0.227121	−0.779564	−2.297086	−3.437506
c_5	−0.008164	−0.005551	−0.004861	−0.002682	−0.005961	−0.006734	0.004916	−0.006480
c_6	0.001246	−0.002836	−0.003579	−0.003295	−0.009524	−0.005579	0.003369	0.003863

The procedure is repeated until χ^2 levels off. In practice, we stop iterations once χ^2 decreases by less than 0.1% in successive steps.

Derivation of Warped Models: T87W

It is important to note that the least squares fitting procedure used to construct the T87W*c* models in this study differs from the procedure used to derive the original T87 and T89 models [*Tsyganenko*, 1990, appendix]. In both cases, the coefficients a_k were determined by least squares fitting using the Levenberg-Marquardt method to advance the "best fitting" coefficients between iterations. The key difference is in the handling of the nonlinear parameters. The derivation of T87 and T89 advanced in stages: it first fixed all nonlinear parameters at some initial guess value and fitted all linear parameters by a standard linear least squares procedure; then it held all linear parameters fixed at their new values and advanced the nonlinear parameters according to the Levenberg-Marquardt method. The procedure was repeated iteratively to minimize the root-mean-squared deviation σ between model and observations. In practice, the largest decrease in σ took place during the first two iterations, and after four or five iterations no further improvement occurred.

By contrast, in the procedure used here to derive T87W*c*, all parameters were advanced together, both linear and nonlinear, according to the Levenberg-Marquardt method. An added feature of our nonlinear least squares fitting program was the use of Singular Value Decomposition (SVD) in the solution of the normal equations (B10), which allowed the freezing of selected eigenvalues during a fitting run (see, for example, section 2.9 of *Press et al.*, [1989]). If the parameters chosen were completely independent of each other, each would correspond to an eigenvalue of the system and thus one would be able to estimate the dependence of σ on that coefficient alone. The actual parameters may, however, have a certain amount of mutual coupling; for instance, in T87*b* [*Tsyganenko*, 1987], the two tail parameters B_1 and B_2 were found to be so strongly linked that B_1 alone contained practically the entire information and hence B_2 was given a fixed value of zero during the fitting process. Thus each eigenvalue is generally made up from a linear combination of model coefficients. The ability to freeze selected eigenvalues allows testing the contribution of each free parameter to a given eigenvalue and lets one identify which parameters are coupled; this is a powerful tool to aid modelers in the search for parameters which are truly independent of each other.

The SVD approach readily provided estimates for the error associated with each of the resulting model parameters through the covariance matrix $C = \alpha^{-1}$. Formally, the elements of the covariance may only be interpreted as the squared standard errors in the parameters derived if the measurement errors are normally distributed. The validity of such assumption was verified by inspection of the difference between the observed and model magnetic fields as illustrated in Table 6. It must be noted that the error estimates derived from the covariance matrix can imply large uncertainties (even exceeding 100%) for some of the parameters. Such enormous error bars are clearly associated with the shallowness of the χ^2 minimum in parameter space and the coupling between parameters discussed above.

The modifications introduced in the T87W model to account for plasma sheet warping have been described by *Peredo and Stern* [1991*b*] but are summarized here for convenience. The T87 tail model responds to tilt angle variations by "tail hinging" through the replacement $z_{GSM} \rightarrow (z_{GSM} - z_s)$, where $z_s = R_H \sin \psi$ and R_H (the "hinging distance") is a constant. Warping effects may be incorporated by allowing z_s to depend on y_{GSM}. For the T87W*c* models used in the present study we have assumed

$$z_s = \begin{cases} \left[(H_0 + D) \sqrt{1 - \left(\dfrac{y_{GSM}}{y_0} \right)^2} - D \right] \sin \psi & |y_{GSM}| \leq y_0 \\ -D \sin \psi & |y_{GSM}| > y_0 \end{cases} \quad \text{(B11)}$$

corresponding to the tail-warping formula of *Fairfield* [1980]. Instead of the original coefficients derived by Fairfield from IMP observations, we have, however, used the coefficients $H_o = 9\ R_E$, $D = 7\ R_E$, and $Y_o = 13.5\ R_E$ derived by *Gosling et al.* [1986] from ISEE data.

Warped models were independently derived for eight magnetic activity ranges corresponding to the ones used to derive the T87*b* model (i.e., the "short" T87 version). The full set of coefficients for the T87W*c* models appear in Table 7. It must be emphasized that these T87W*c* models were derived from ISEE data alone and thus are not valid tailward of $x \approx -22\ R_E$.

Acknowledgments. This work was performed while one of us (N.A.T.) held a National Research Council-NASA/Goddard Space Flight Center Research Associateship. The authors are indebted to C. Huang for providing copies of her results as well as many stimulating discussions. Fruitful discussions with D. H. Fairfield are gratefully acknowledged. Thanks are also due to M. V. Malkov for his invaluable help in creating the ISEE modeling data sets.

The Editor thanks two referees for their assistance in evaluating this paper.

REFERENCES

Bevington, P. R., *Data Reduction and Error Analysis for the Physical Sciences*, McGraw-Hill, New York, 1969.

Donovan, E., G. Rostoker, and C. Y. Huang, Regions of negative B_z in the Tsyganenko 1989 model neutral sheet, *J. Geophys. Res.*, *97*, 8697, 1992.

Fairfield, D. H., A statistical determination of the shape and position of the geomagnetic neutral sheet, *J. Geophys. Res.*, *85*, 775, 1980.

Fairfield, D. H., The magnetic field of equatorial magnetotail from 10 to 40 R_E, *J. Geophys. Res.*, *91*, 4238, 1986.

Fairfield, D. H., An evaluation of the Tsyganenko magnetic field model, *J. Geophys. Res.*, *96*, 1481, 1991.

Fairfield, D. H., M. H. Acuña, L. J. Zanetti, and T. A. Potemra, The magnetic field of the equatorial magnetotail: AMPTE/CCE observations at R < 8.8 R_E, *J. Geophys. Res.*, *92*, 7432, 1987.

Gosling, J. T., D. J. McComas, M. F. Thomsen, S. J. Bame, and C. T. Russell, The warped neutral sheet and plasma sheet in the near-earth geomagnetic tail, *J. Geophys. Res.*, *91*, 7093, 1986.

Huang, C. Y., G. Rostoker, and L. A. Frank, The plasma sheet magnetic field during varying phases of geomagnetic activity (abstract), *Eos Trans. AGU*, *71*(43), 1545, 1990.

Huang, C. Y., G. Rostoker, and L. A. Frank, The magnetic field in the neutral sheet of the magnetotail (abstract), *Eos Trans. AGU*, *72*(17), Spring Meeting suppl., 243, 1991.

Kayser, S. E., and D. H. Fairfield, Comparison of the Tsyganenko 1987 and 1989 magnetospheric models with observations (abstract), *Eos Trans. AGU*, *72*(17), Spring Meeting suppl., 255, 1991.

Marquardt, D. W., An algorithm for least-squares estimation of nonlinear parameters, *J. Soc. Indust. Appl. Math.*, *11*, 431, 1963.

Peredo, M., and D. P. Stern, The magnetic field in the geotail: Magnetospheric models and observations (abstract), *Eos Trans. AGU*, *72*(44), Fall Meeting suppl., 395, 1991*a*.

Peredo, M., and D. P. Stern, On the position of the near-earth neutral sheet: A comparison of magnetic model predictions with empirical formulas, *J. Geophys. Res.*, *96*, 19,521, 1991*b*.

Peredo, M., N. A. Tsyganenko, S. A. Curtis, D. P. Stern, and M. V. Malkov, Solar wind and IMF control of the magnetopause in a Tsyganenko model with tail warping (abstract), *Eos Trans. AGU*, *73*(43), Fall Meeting suppl., 462, 1992.

Press, W. H., B. P. Flannery, S. A. Teukolsky, and W. T. Vetterling, *Numerical Recipes*, Cambridge University Press, New York, 1989.

Rostoker, G., and S. Skone, Magnetic flux mapping considerations in the auroral oval and the earth's magnetotail, *J. Geophys. Res.*, *98*, 1377, 1993.

Sibeck, D., R. Lopez, and E. Roelof, Solar wind control of the magnetopause shape, location and motion, *J. Geophys. Res.*, *96*, 5489, 1991.

Speiser, T. W., and N. F. Ness, The neutral sheet in the geomagnetic tail: Its motion, equivalent currents, and field line connection through it, *J. Geophys. Res.*, *72*, 131, 1967.

Stern, D. P., A model of the magnetospheric tail with current-free lobes, *Planet. Space Sci.*, *38*, 255, 1990.

Stern, D. P., and N. A. Tsyganenko, Uses and limitations of the Tsyganenko magnetic field models, *Eos Trans. AGU*, *73*(46), 489, 1992.

Tsyganenko, N. A., Global quantitative models of the geomagnetic field in the cislunar magnetosphere for different disturbance levels, *Planet. Space Sci.*, *35*, 1347, 1987*a*.

Tsyganenko, N. A., Average statistical structure of the magnetotail according to satellite data, *Geomagn. Aeron.*, *27*, 854, 1987*b*.

Tsyganenko, N. A., A magnetospheric magnetic field model with a warped tail current sheet, *Planet. Space Sci.*, *37*, 5, 1989.

Tsyganenko, N. A., Quantitative models of the magnetospheric magnetic field: Methods and results, *Space Sci. Rev.*, *54*, 75, 1990.

Tsyganenko, N. A., and A. V. Usmanov, Determination of the magnetospheric current system parameters and development of experimental geomagnetic field models based on data from IMP and HEOS satellites, *Planet. Space Sci.*, *30*, 985, 1982.

Tsyganenko, N. A., M. V. Malkov, D. P. Stern, and M. Peredo, Magnetospheric magnetic field structure from and IMP-HEOS-ISEE data set and its dependence on the solar wind state (abstract), *Eos Trans. AGU*, *73*(14), Spring Meeting suppl., 256, 1992.

M. Peredo, Hughes STX Corporation at NASA/Goddard Space Flight Center, Laboratory of Extraterrestrial Physics, Code 695, Greenbelt, MD 20771.

D. P. Stern and N. A. Tsyganenko, NASA Goddard Space Flight Center, Laboratory for Extraterrestrial Physics, Code 695, Greenbelt, MD 20771.

(Received October 26, 1992;
revised March 9, 1993;
accepted April 19, 1993.)